Optical Engineering

OpticalEngineering.SPIEDigitalLibrary.org

Incoherent imaging in the presence of unwanted laser radiation: vortex and axicon wavefront coding

Abbie T. Watnik
Garreth J. Ruane
Grover A. Swartzlander, Jr.

SPIE.

Abbie T. Watnik, Garreth J. Ruane, Grover A. Swartzlander, Jr. "Incoherent imaging in the presence of unwanted laser radiation: vortex and axicon wavefront coding," *Opt. Eng.* **55**(12), 123102 (2016), doi: 10.1117/1.OE.55.12.123102.

Incoherent imaging in the presence of unwanted laser radiation: vortex and axicon wavefront coding

Abbie T. Watnik,[a,*] Garreth J. Ruane,[b] and Grover A. Swartzlander Jr.[b]
[a]U.S. Naval Research Laboratory, 4555 Overlook Avenue Southwest, Washington, DC 20375, United States
[b]Rochester Institute of Technology, Chester F. Carlson Center for Imaging Science, 54 Lomb Memorial Drive, Rochester, New York 14623, United States

Abstract. Vortex and axicon phase masks are introduced to the pupil plane of an imaging system, altering both the point spread function and optical transfer function for monochromatic and broadband coherent and incoherent light. Each phase mask results in the reduction of the maximum irradiance of a localized coherent laser source, while simultaneously allowing for the recovery of the incoherent background scene. We describe the optical system, image processing, and resulting recovered images obtained through this wavefront encoding approach for laser suppression. [DOI: 10.1117/1.OE.55.12.123102]

Keywords: imaging systems; phase-only filters; deconvolution; wavefront encoding.

Paper 160495 received Apr. 4, 2016; accepted for publication Nov. 4, 2016; published online Dec. 7, 2016.

1 Introduction

Wavefront coding is the process of introducing a phase mask in the pupil plane of an optical system and recovering an image through digital processing. Such optical systems are designed by jointly considering the optical system and the image processing for a specific function or application. For example, wavefront coding has been used for extending the depth of focus with a cubic phase mask.[1–3]

The application of our work is to reduce the risk of laser damage from coherent laser sources. In a traditional imaging system, a distant laser source will be focused onto the focal plane of the optical system. The focused beam may cause laser dazzle across the sensor, blinding the sensor from the background incoherent image of interest.[4] What is more, the sensor may suffer single or multiple pixel surface damage, crystal cleavage and/or cracking, or permanent physical damage between the detector and the readout electronics.[5]

Nonlinear optical limiters have been introduced to mitigate sensor damage.[6–9] Optical limiters may block all light to the sensor and the desired background image can no longer be recovered; additionally, narrow bandwidths are required.

In our approach, we investigate the use of higher-order vortex and axicon phase masks in the pupil plane of the imaging system to redistribute the coherent laser light away from a tight focal spot, thereby reducing the irradiance on individual pixels while also allowing for the recovery of the background image. We previously outlined the theory and presented initial results.[10] In this paper, we alter the sensor configuration and utilize higher-order phase mask designs to demonstrate four orders of magnitude of laser suppression for vortex and axicon phase masks. A discussion of the optical system design and image recovery is provided. We examine and compare the coherent point spread function (PSF) and incoherent modulation transfer function (MTF) properties of the phase masks, which yield high suppression of coherent light and successful image recovery of incoherent background images, respectively. Simulated results are presented for reconstructed incoherent images in the presence of laser sources for several cases including noise and noiseless conditions as well as monochromatic and broadband illumination conditions.

In Secs. 1–6 of the paper, we will assume quasimonochromatic light for the background image (i.e., the bandwidth is much smaller than the center frequency), and a laser wavelength that is within this bandwidth range. In Sec. 7, we present results and discussion regarding broadband source illumination.

2 Optical System

Figure 1 shows the imaging chain with both the physical optical system and the image processing steps that allow the recovery of an incoherent background image in the presence of a coherent laser source. The optical system consists of a phase mask, $t(x,y)$, in the pupil plane of the imaging system and an adjacent imaging lens, followed by a focal plane imaging sensor in the (x',y') plane. A vortex phase element has a complex transmittance

$$t_v(x,y) = \exp(im\theta), \tag{1}$$

where m is a nonzero integer known as the topological charge. An axicon phase element has a complex transmittance of

$$t_a(x,y) = \exp(ir/a), \tag{2}$$

where a is a constant scaling length. In this report, we ignore any wavelength dependence of m and a. The coordinates (r,θ) are the circular coordinates in the (x,y) plane. The irradiance in the sensor plane may be expressed $I(x',y',\lambda) = I_L(x',y',\lambda_L) + I_b(x',y',\lambda_b)$, where the contribution from the laser source $I_L(x',y',\lambda_L)$ and the background scene $I_b(x',y',\lambda_b)$ are given by

*Address all correspondence to: Abbie T. Watnik, E-mail: abbie.watnik@nrl.navy.mil

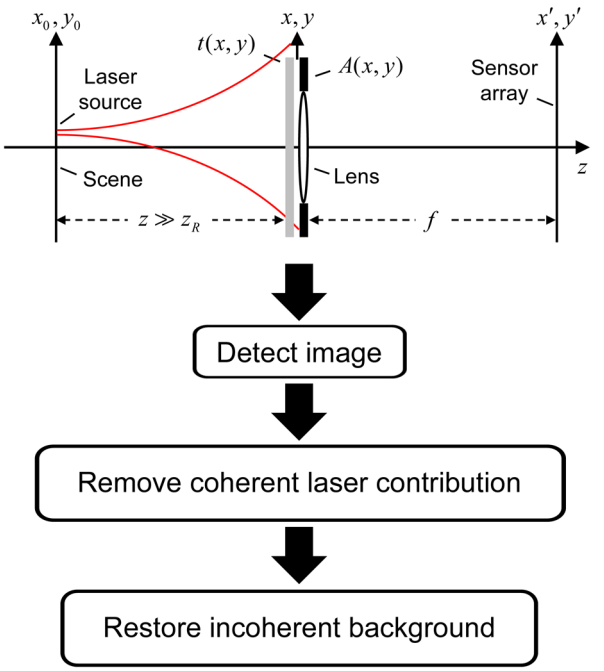

Fig. 1 The imaging chain includes both a physical optical system as well as several postprocessing steps.

$$I_L(x', y', \lambda_L) = \alpha |U_g(x', y', \lambda_L) * h(x', y', \lambda_L)|^2, \tag{3}$$

and

$$I_b(x', y', \lambda_b) = \beta [b_g(x', y', \lambda_b) * |h(x', y', \lambda_b)|^2], \tag{4}$$

where α and β are the constants, $U_g(x', y', \lambda_L)$ and $b_g(x', y', \lambda_b)$ are the geometrically imaged fields of the laser source and background scene, respectively, and $h(x', y', \lambda)$ is the complex PSF of the optical system given by the Fourier transform of the pupil function

$$\begin{aligned} h(x', y', \lambda) &= \mathrm{FT}\{A(x,y)t(x,y)\} \\ &= \int_{-\infty}^{\infty}\int_{-\infty}^{\infty} A(x,y)t(x,y) \\ &\quad \times \exp\left[-i\frac{2\pi}{\lambda f}(x'x + y'y)\right] \mathrm{d}x\,\mathrm{d}y, \end{aligned} \tag{5}$$

and the aperture function is assumed to be circular with a radius R; i.e., $A(x,y) = \mathrm{circ}(r/R)$. Analytical closed form expressions of the PSF of the vortex and axicon phase masks can be found in Refs. 11–13. For simplicity, we will make all calculations at the center wavelength, λ, and drop the use of λ_L and λ_b.

Equations (3) and (4) analytically distinguish the differences between coherent and incoherent imaging. Coherent image formation is linear in complex field, while incoherent image formation is linear in intensity. Coherent and incoherent light have different transfer functions, h and $|h|^2$, respectively, which afford an opportunity to separate the contributions after detection, especially if given some *a priori* knowledge of the imaging scenario. The laser source is assumed to be small and located far enough away from the aperture of the system that the beam width becomes large with respect to the system aperture and hence the lens is evenly illuminated. Breakdowns in the assumptions of the properties of the coherent beam (atmospheric turbulence effects) may affect the ability to separate the coherent and incoherent detected irradiance image. Solutions to handle such cases are discussed in Sec. 6 of Ref. 10.

With a phase mask in the pupil plane of the imaging system, we are seeking to accomplish two (not necessarily mutually related) goals: (1) coherent contribution: reduce the maximum irradiance of the PSF and (2) incoherent contribution: recover the incoherent image after deconvolution. A diffraction-limited optical system will concentrate the incoming laser light, which is contrary to goal 1. Intuitively, we would like to introduce a pupil phase mask that spreads light across as many pixels as possible. In the extreme case, the PSF would uniformly illuminate the image plane, such that maximum irradiance would be equal to the mean irradiance. This approach, however, is not amenable to goal 2. From the perspective of the incoherent contribution, we need to consider how the phase mask changes the optical transfer function (OTF) and suppresses the spatial frequencies of the incoherent image. Zeroes in the spatial frequencies in the OTF result in the loss of information, and thus the original image cannot be completely recovered by means of deconvolution techniques.

We seek to determine what types of phase masks can simultaneously address both coherent and incoherent criteria. Within the context of this paper, we will explore the properties of vortex and axicon pupil phase masks and elucidate why their unique characteristics achieve the stated criteria for both the coherent and incoherent contributions.

3 Why Vortex and Axicon Pupil Phase Masks

Vortex and axicon pupil phase masks result in "donut"-like coherent PSFs. Although these phase functions do not induce uniform spreading of the light throughout the image plane, the beam energy is redistributed over a large area and thus the maximum irradiance is reduced. The larger the ring, the greater the reduction of the maximum irradiance at a single pixel. Additionally, the sharp features of the "donut" ring (distinct edge between central region and ring) mean that the OTF will contain high spatial frequency content. Figure 2 shows side-by-side the vortex and axicon pupil phase masks and line profiles of the PSF and the MTF for a simulated example case where the maximum irradiance of the PSF is matched (e.g., $I_{\max}/I_o = 2.3 \times 10^{-3}$, where $I_{\max}$ is the PSF irradiance with the phase element and I_o is the PSF irradiance without a phase element). The ratio $I_{\max}/I_o$ signifies the reduction in laser irradiance at the focal plane with the phase plate present. The specific peak suppression ratio shown in Fig. 2 is due to the vortex phase mask with $m = 40$ or an axicon phase mask with $a = R/124$. These values were chosen to demonstrate equivalent irradiance suppression of 3 orders of magnitude with the two different phase masks. Further details of the imaging properties are included in Sec. 5 where we explore high-order vortex and axicon pupil phase masks. The unique attributes of the vortex and axicon pupil plane phase masks for both the coherent and incoherent imaging conditions make both phase patterns good candidates for wavefront coding in our specification application, which we explore through a computational experiment.

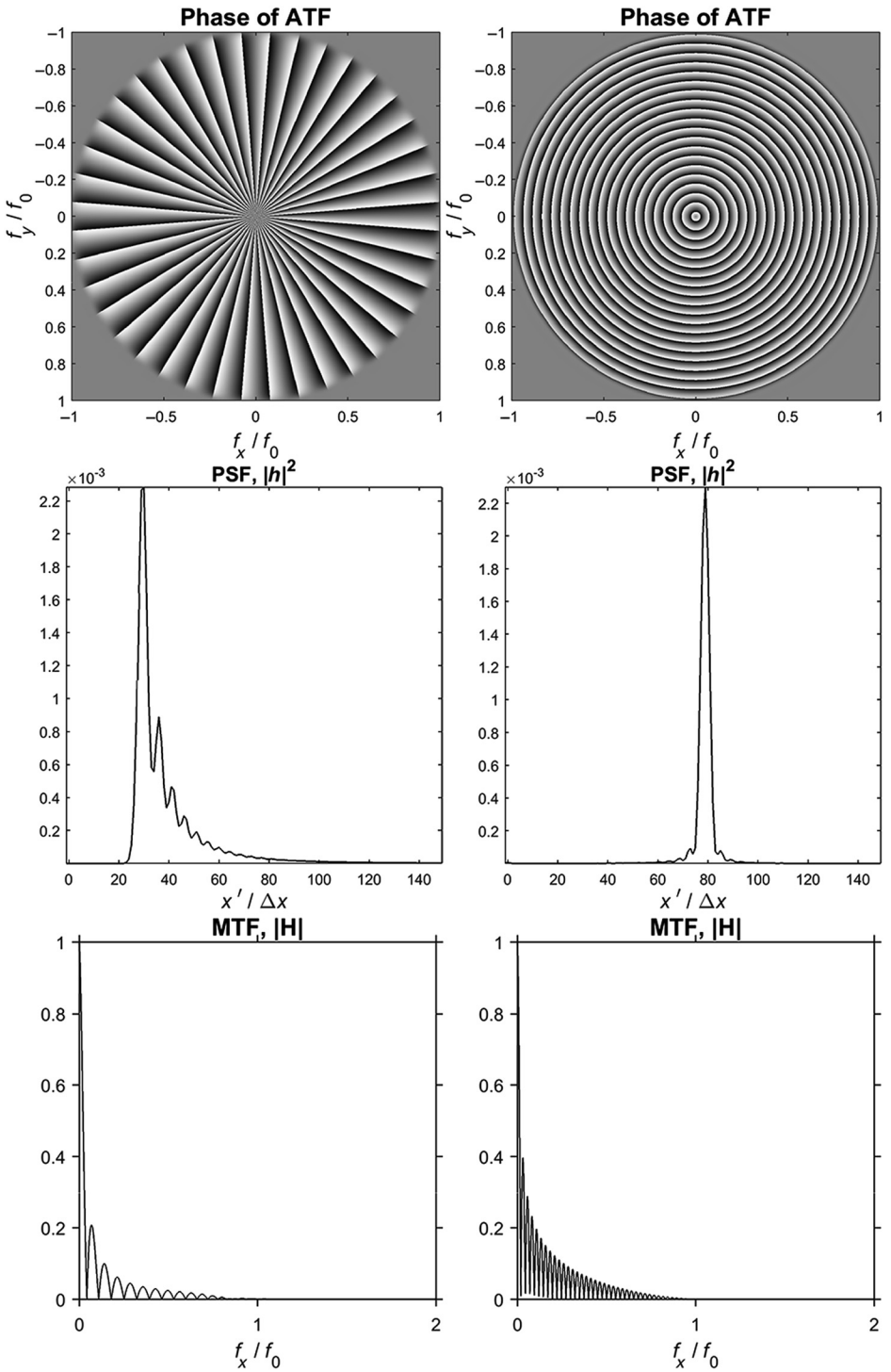

Fig. 2 Example of (a) high-order vortex ($m = 40$) and (b) axicon ($a = R/124$) amplitude transfer function phase masks with corresponding normalized PSF irradiance profiles and MTF profiles. Grayscale ranges over mod(2π). The PSF line profiles are normalized such that the maximum irradiance without a phase element is unity. PSF and MTF plots are symmetric about the origin $f_o = R/(\lambda f)$.

4 Modeling Parameters

4.1 *Imaging Scene*

We model a physical optical system to establish the concept of high-order vortex and axicon phase plate wavefront encoding of quasimonochromatic incoherent and coherent illumination. The pupil plane is a circular aperture with a 2048 pixel diameter embedded in a 4096×4096 pixel array, yielding a detector sampling rate of $Q = 2$. The geometric image was 2048×2048 pixels embedded in the 4096×4096 pixel array. The geometric image was quantized with 16-bits. No noise or atmospheric turbulence effects were included since the primary focus of this work is to solely evaluate the presence of high-order phase masks; results with noise will be discussed separately in Sec. 6. The detected image consists of contributions from an unwanted

bright laser source $I_L(x', y')$ and a relatively dim spatially incoherent background image $I_b(x', y')$.

The geometric image of the incoherent background image is shown in Fig. 3. The mean incoherent image signal is a quarter of the well depth of the sensor, $\langle I_b(x, y)\rangle = 2^{16}/4$ digital counts. The camera saturates at full well depth. We define the laser brightness as a ratio of focused laser light I_o (with no phase mask in imaging system) to the camera saturation I_{sat}

$$I_o/I_{\text{sat}} = 2 \times 10^3. \tag{6}$$

We chose the given ratio to illustrate a scenario with a bright laser source several orders of magnitude greater than the camera saturation.

Line profiles from the coherent (laser) normalized PSF intensity are shown in Fig. 4 for various masks. The vortex PSF is shown in blue and the axicon PSF is shown in red. Line profiles in each subplot have equivalent maximum intensity. Figure 4(a) shows plots with $I_{\max}/I_o = 2.2 \times 10^{-2}$, where I_o is the PSF intensity without a phase mask present. The mask parameters were set to $m = 10$ for the vortex phase element and $a = R/15$ for the axicon.

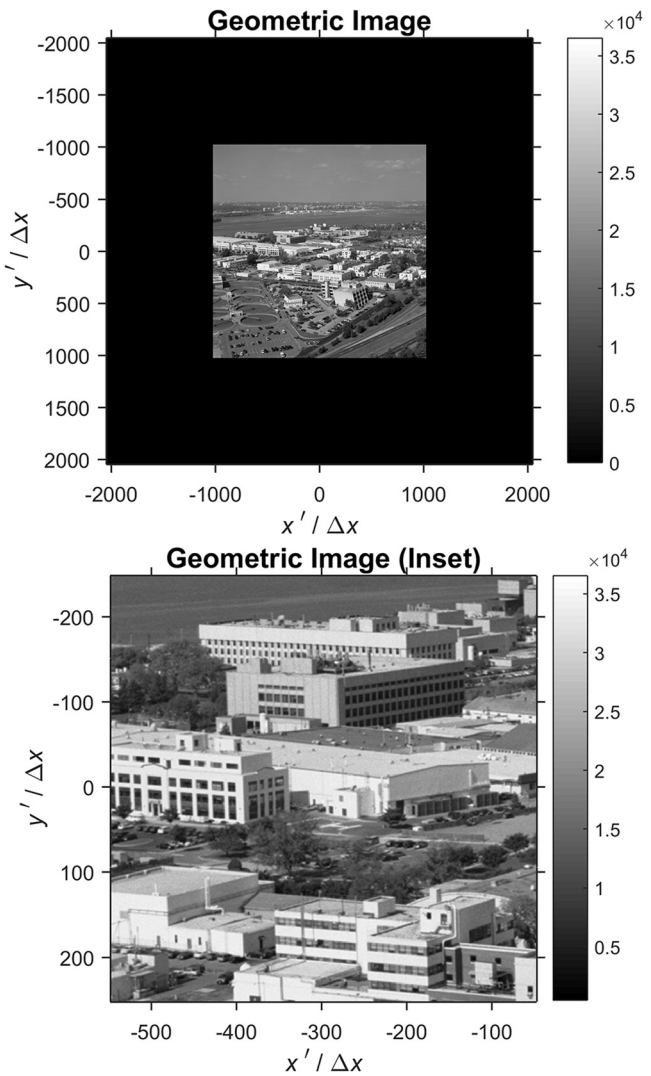

Fig. 3 Geometric image of the incoherent background scene without wavefront encoding (ideal case).

In Fig. 4(b), $I_{\max}/I_o = 2.3 \times 10^{-3}$, $m = 40$, and $a = R/124$ and in Fig. 4(c), $I_{\max}/I_o = 2.9 \times 10^{-4}$, $m = 120$, and $a = R/1004$. Figure 4 also shows a black horizontal line denoting the saturation level of the camera compared to the PSF functions of vortex and axicon phase plates. Note that in Fig. 4(a), the maximum laser irradiance is well above the saturation level; in Fig. 4(b), the maximum laser irradiance is slightly above saturation, and in Fig. 4(c), the maximum laser irradiance is below saturation. All the pixels above the saturation level are thresholded to the

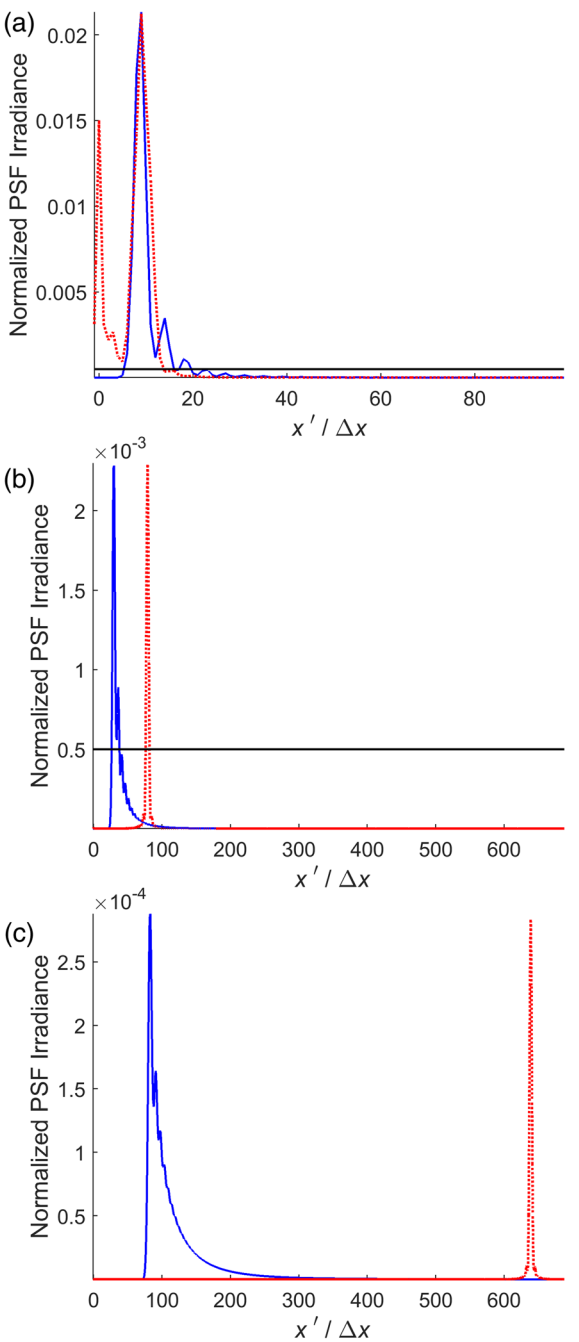

Fig. 4 Normalized PSF irradiance profiles for vortex phase plates (blue, solid), where (a) $m = 10$, (b) 40 (middle), and (c) 120 (bottom); for axicon phase plate (red, dotted) where $a/R = 1/15$ (top), $1/124$ (middle), and $1/1004$ (bottom). Note scale differences between plots. Black horizontal line shows the saturation level of the camera compared to the PSF intensity.

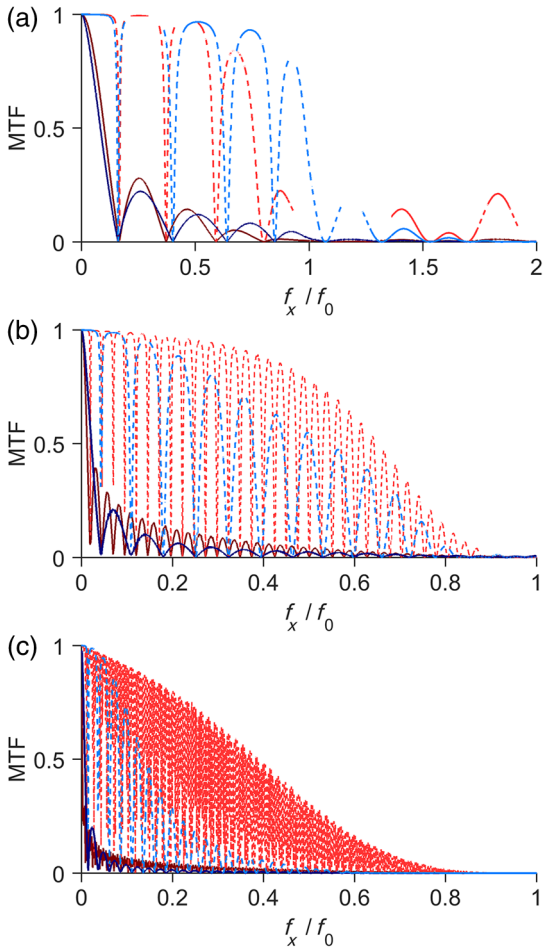

Fig. 5 MTF profiles for detected (solid) and reconstructed after Wiener filtering (dashed) for vortex phase plates (blue), where (a) $m = 10$, (b) 40, and (c) 120; for axicon phase plate (red), where (a) $a/R = 1/15$, (b) $1/124$, and (c) $1/1004$. Vortex = dark blue/light blue and axicon = dark red/light red. $f_0 = R/\lambda f$. Note scale differences between plots.

maximum pixel well depth. The MTFs corresponding to each of the PSFs in Fig. 4 are shown in Fig. 5 before and after Wiener deconvolution (described in Sec. 4.3).

The corresponding detected scenes are shown in Fig. 6 in the upper two rows. The top row shows the full 4096×4096 pixel array in the sensor plane, while the second row shows a cropped 500×500 pixel portion within the array. Areas of saturation are visible for the detected images with $m = 10$, $a = R/15$, $m = 40$, and $a = R/124$.

4.2 *Laser Subtraction*

After detection of the incoming light on the sensor from the wavefront-encoded optical system, image postprocessing must be performed to reconstruct the incoherent background image. The first step in the postprocessing is the removal of the coherent laser source. The contribution of the laser source is estimated from the known phase mask in the optical system and optimized for size, location, and brightness in the detected image using a Nelder–Mead simplex algorithm[14,15] until the estimated laser contribution base matches the detected image. The estimation process allows for a partially saturated image. Once the coherent laser irradiance is subtracted, the area of the image that was saturated will have zero value; information has been lost and cannot be directly recovered. However, to reduce ringing in the reconstruction, we choose to substitute the mean signal value in this region. The third row in Fig. 6 shows the inset images after the laser source position and brightness has been estimated and removed, and the mean signal value is substituted in the saturation regions.

4.3 *Incoherent Image Restoration*

After removal of the coherent laser contribution, the remaining intensity is that of the incoherent background image, blurred by the optical system's phase mask. Wiener deconvolution is used to reconstruct the background scene with the following filter:

$$W(k\Delta\xi, p\Delta\eta) = \frac{\mathcal{H}^*(k\Delta\xi, p\Delta\eta)}{|\mathcal{H}(k\Delta\xi, p\Delta\eta)|^2 + 1/\mathrm{SNR}}, \tag{7}$$

where (k, p) are the spatial frequency indices, $\Delta\xi = 1/(N\Delta x)$, $\Delta\eta = 1/(M\Delta x)$, and SNR is the signal-to-noise ratio. In this simulation, we set $1/\mathrm{SNR} = 5 \times 10^{-4}$. The last row in Fig. 6 depicts the reconstructed images after image processing. Note that in the images where areas of saturation were present due to the laser source, some ringing artifacts are present due to Wiener deconvolution of the sharp edge between the saturated region and incoherent image, but only impact the immediate area around the saturated region. The SNR term in the Wiener filter can be adjusted to reduce the ringing effect, with sacrifice to the reconstructed image sharpness. Alternatively, a smoother, apodized boundary between the known irradiance and the saturated regions would lessen ringing effects as well. Since the ringing artifacts only impact the immediate area around the saturated region and not the entire extent of the image, we have not focused on reducing the ringing artifacts in this work.

5 Optical System Modifications for Higher-Order Phase Masks

5.1 *Coherent Contributions*

We see in Fig. 4 the PSF intensity line profiles of the coherent laser light. Initial observations from these plots show that both types of phase masks exhibit "donut"-like PSF functions; light is concentrated in a ring. With higher-order masks, the ring diameter expands, and thus the maximum intensity decreases since total power is preserved. The vortex profile exhibits a $1/r^2$ falloff around the intensity ring maximum,[16] while the axicon PSF profile is a narrow ring. Due to the difference in the $1/r^2$ falloff of the vortex profile and the narrow ring of the axicon profile, the diameter of the axicon ring grows more quickly than the vortex ring at higher level of intensity suppression. In effect, the "donut" ring has an increased width for the vortex-encoded PSF. For the axicon-encoded PSF with $a = R/15$, most of the PSF structure is above the saturation level, and after clipping, a near-solid circular region is saturated. For the highest-order phase plates presented in this paper [see Fig. 4(c)], the pupil phase encoding with both vortex and axicon plates reduces the normalized PSF intensity below the saturation level of the camera.

In designing the imaging system, we want to ensure that all light from the pupil plane falls on the focal plane imaging

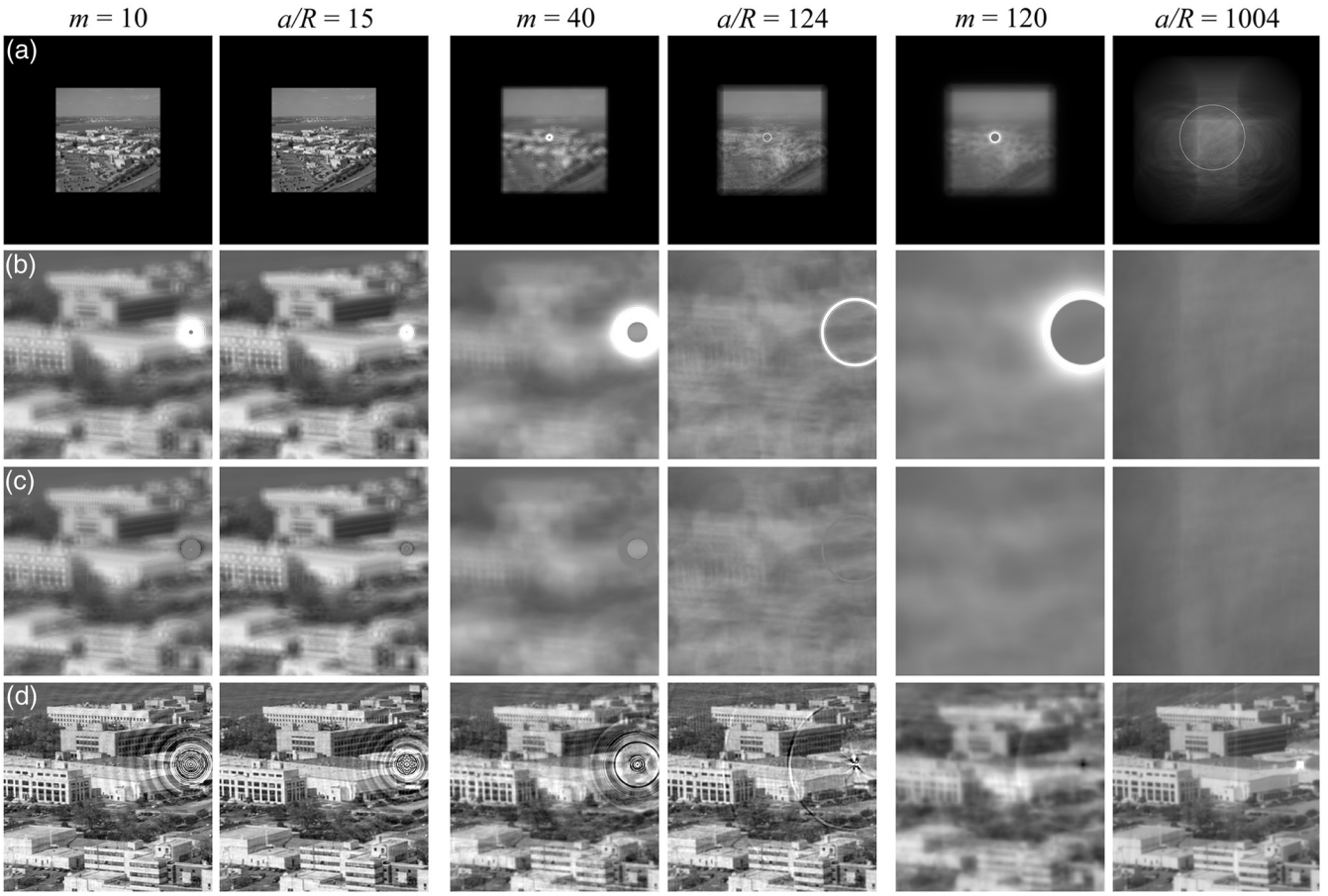

Fig. 6 Image processing steps after wavefront encoding with vortex and axicon pupil phase functions: (a) detected image, (b) detected image (cropped 500×500 pixel section), (c) detected image section after laser subtraction and substitution of mean signal in saturated regions, and (d) final cropped image after deconvolution.

sensor. If light falls off the sensor, information will be lost, and there will be severe issues with the image reconstruction. With the spread of light, as evidenced by the PSF functions shown in Fig. 4, clipping of the image is likely if the imager has been designed as a no-mask, diffraction-limited imager. Now, instead of designing based on an in-focus image that fills the sensor, we are designing based on a wavefront-encoded image that fills the sensor. We start by considering the coherent laser source and its spreading PSF. The position of the laser source of the focal plane is unknown. For an in-focus image, the laser source could damage any pixel in an $N \times N$ array. With the phase plate included, the size of the array must now be $\sim[N + 650 \text{ pixels}] \times [N + 650 \text{ pixels}]$, as determined by spread of the axicon PSF with 4 orders of magnitude reduction in maximum intensity [see Fig. 4(c)]. Note that with a vortex phase plate, the increase in array size is smaller, approximately $\sim[N + 200 \text{ pixels}] \times [N + 200 \text{ pixels}]$.

The impact of sensor size on image quality must be considered. When designing the optical system, one is usually constrained by available sensor sizes. Therefore for a given sensor size, to accommodate the spread of the blur, the size of the in-focus image is reduced, or equivalently, there is a reduction in resolution or field of view compared to an in-focus image that fills the same sensor size. When calculating the resolution or an image quality metric, comparison to the original imagery must be taken into account.

5.2 *Incoherent Contributions: Spatial Frequency Analysis*

The pupil phase mask not only suppresses the coherent laser light from the laser source, but it simultaneously impacts the incoherent background scene. As shown in Eq. (4), the detected irradiance of the background scene is the convolution of the geometric image of the background scene with the magnitude-squared of the complex PSF function, or equivalently the Fourier transform of the system OTF. The modulus of the OTF is the MTF; the MTF line profiles for the vortex and axicon phase plates with the parameters described in Sec. 3 are shown in Fig. 5. The solid line profiles denote the MTF functions for a given phase mask in the pupil plane. Both the vortex and axicon phase masks result in zeros in the MTF spatial frequency plots. With higher-order phases, the vortex MTF profiles (shown in blue) exhibit less zeros but a lower magnitude of the underlying envelope than the axicon MTF profiles (shown in red). The dotted lines are profiles of the MTF function after Wiener filtering. The result of Wiener filtering, as clearly demonstrated here, is to boost the spatial frequencies of the MTF. The image quality of the reconstructed images shown in the bottom row in Fig. 6 can be quantitatively assessed by the cutoff frequency of the boosted MTF functions. Figure 5(a) shows the cutoff frequency of the vortex-encoded image to be near $f_x = 1.5 \times f_o$; the MTF of the axicon-encoded image has a null region from $f_x = f_o$ to

$f_x = 1.25 \times f_o$, but then a high-frequency boost up for $f_x = 2 \times f_o$. Spatial frequency $f_0 = R/\lambda f$ is referred to as the coherent cutoff spatial frequency, whereas twice that value is the incoherent cutoff spatial frequency. The cutoff spatial frequency in Fig. 5(b) is $f_x = 0.8 \times f_o$ and $f_x = 0.9 \times f_o$ for the vortex- and axicon-encoded images, respectively.

For the highest-order phase masks used in this work, we see a substantial difference between the vortex- and axicon-encoded restored MTF functions. The boosted signal of the vortex-encoded MTF has a reduced amplitude and a cutoff spatial frequency near $f_x = 0.5 \times f_o$, while the Wiener-boosted signal of the axicon-encoded MTF has a cutoff spatial frequency near $f_x = 0.8 \times f_o$. The combination of smaller amplitude and a reduced cutoff spatial frequency results in a visually noticeable difference in the image quality between the vortex- and axicon-encoded images, shown in Fig. 6.

Overall, the MTF functions of these wavefront-encoded incoherent images show that for higher-order phase functions, the maximum cutoff frequency decreases, resulting in poorer image quality. Zeros in the MTF also pose a difficulty in Wiener filtering image processing because no information remains for that given spatial frequency; Wiener filtering can only boost the signal of nonzero spatial frequencies. With the highest-order phase masks presented where $m = 120$ and $a = R/1004$, the axicon-encoded image showed better image quality after image processing by Wiener filtering.

6 Effect of Noise

We repeated the experiments keeping all the parameters the same, but including the presence of both photon-counting and Gaussian detector noise. The Gaussian noise had a mean and standard deviation of 10 counts. The noise introduces slight errors into the reconstruction in two ways, namely, (1) the subtraction of the coherent laser contribution and (2) the incoherent deconvolution. Figure 7 shows a comparison between noise and noiseless reconstructions for $m = 120$ and $a = R/124$. Results are comparable for the other phase masks described in this paper when noise is introduced (not shown). At these given levels of noise, the reconstructed image is not significantly affected by the subtraction of the coherent laser source or the image deconvolution.

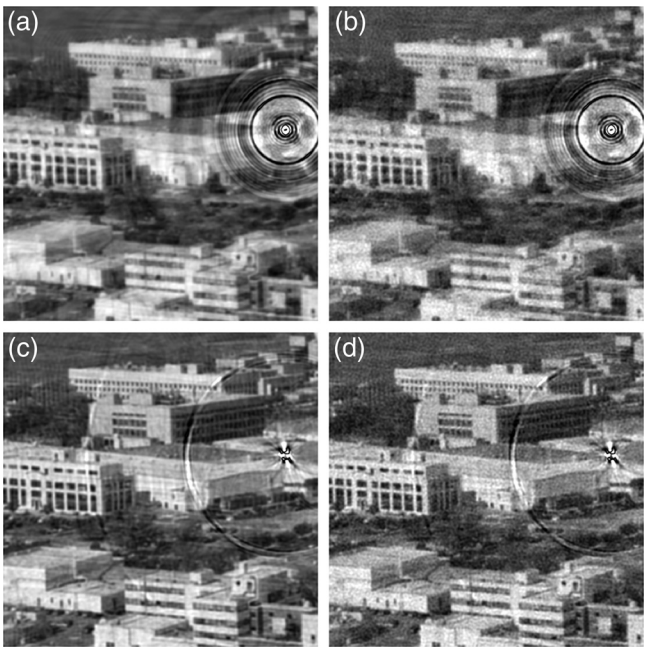

Fig. 7 Comparison between final cropped image after deconvolution for noiseless and noise cases: (a) vortex phase mask, $m = 40$, noiseless and (b) vortex phase mask, $m = 40$, with noise. (c) Axicon phase mask, $a/R = 124$, noiseless and (d) axicon phase mask, $a/R = 124$, with noise.

7 Multiwavelength Illumination

The results shown in this paper consider a quasimonochromatic imaging scenario. Here in Sec. 7, we present how this approach can also be adapted for polychromatic imaging in the presence of a coherent laser. The PSF scales with wavelength, which affects both the detected image irradiance and the image reconstruction processes. The polychromatic PSF is the incoherent sum of quasimonochromatic PSFs over the passband, namely

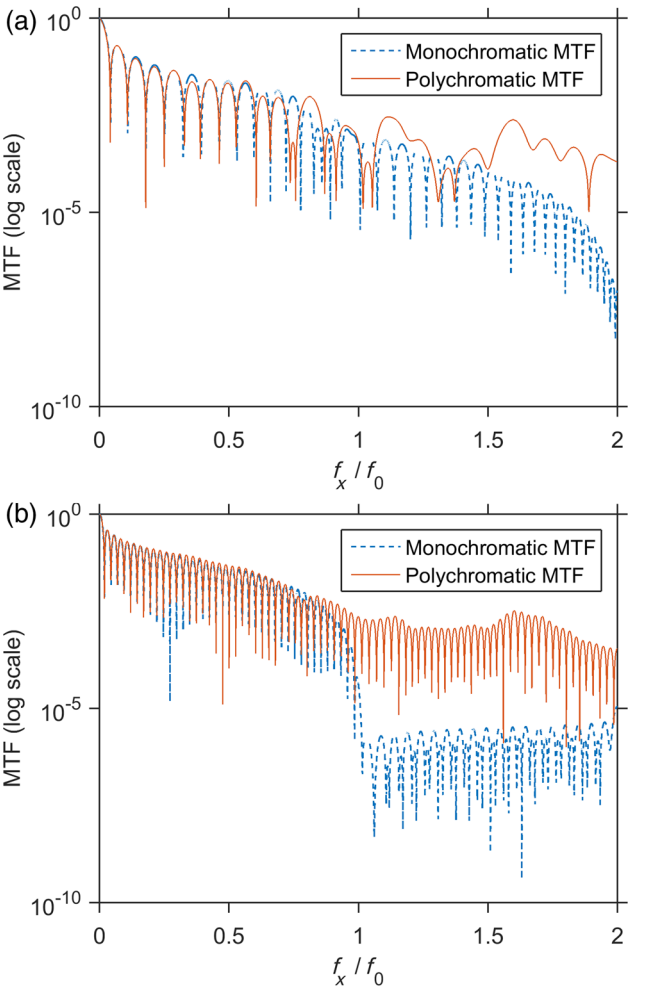

Fig. 8 MTF profiles of monochromatic illumination (dotted line) at $\lambda = 600$ nm and polychromatic illumination (solid line) with a bandwidth of $\Delta\lambda = 500 - 700$ nm for a vortex phase mask, where $m = 40$ (top) and an axicon phase mask $a/R = 1/124$ (bottom). $f_0 = R/\lambda f$. Plots shown on a logarithmic scale.

$$\tilde{h}^2(x', y') = (1/\Delta\lambda) \int_{\Delta\lambda} w(\lambda)|h(x', y', \lambda)|^2 \mathrm{d}\lambda, \quad (8)$$

where $w(\lambda)$ is the spectral weighting function and $h(x', y', \lambda)$ is the PSF for a specific wavelength.

As described in Sec. 4.2, our approach for laser subtraction estimates the size, location, and brightness of the monochromatic coherent PSF, given the known aperture and phase mask of the system. For the broadband case, the laser subtraction approach is modified to account for optimization with respect to the polychromatic PSF on the focal plane. Once the laser contribution is subtracted, the polychromatic incoherent background remains. Deconvolution of the incoherent background with a polychromatic PSF may be used.[17] In Fig. 8, we plot the monochromatic and polychromatic MTF functions on a logarithmic scale for the vortex and axicon, $m = 120$ and $a = R/124$, respectively. Note that there are minimal differences to the MTF for lower spatial frequencies, and the MTF at higher spatial frequencies is actually improved. Figure 9(a) shows a comparison between the monochromatic and broadband ($\Delta\lambda = 500 - 700$ nm) incoherent image reconstructions for a subset of the full image after the laser component is removed for a vortex phase mask, $m = 120$, while Fig. 9(b) shows the equivalent reconstruction for an axicon phase mask, $a = R/124$. The reconstructed area around the saturated laser has slight differences between the monochromatic and broadband cases for the vortex phase mask; the monochromatic case shows more fine-scale ringing effects that are not present in the broadband case. The underlying incoherent background image is comparable for the monochromatic and broadband cases, suggesting negligible effects for broadband reconstructions.

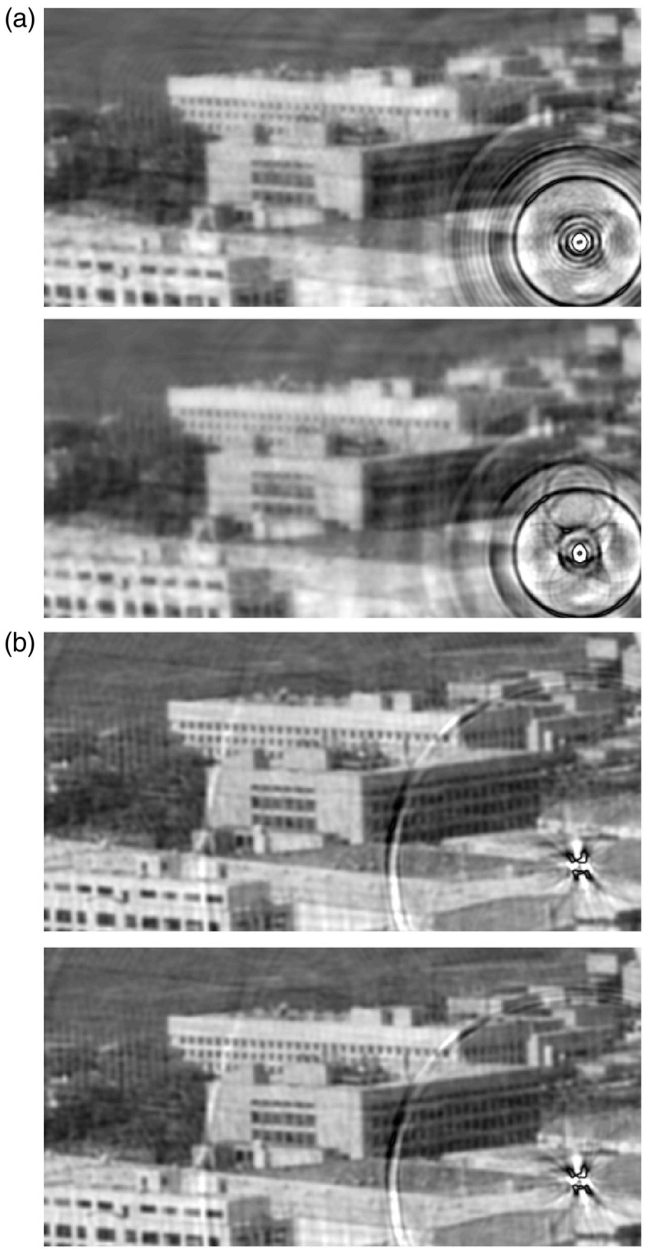

Fig. 9 Comparison between final cropped image after deconvolution for monochromatic ($\lambda = 600$ nm) and polychromatic ($\Delta\lambda = 500 - 700$ nm) cases. (a) Vortex phase mask, $m = 40$, monochromatic/polychromatic and (b) axicon phase mask, $a/R = 124$, monochromatic/polychromatic.

8 Summary

In this paper, we have shown that incoherent background scenes can be restored in the presence of an intense laser source with high-order wavefront coding for both vortex and axicon pupil phase masks. The higher-order phase elements introduced more blurring to the coherent and incoherent scene, decreasing the maximum laser irradiance in the detected image, and thereby reducing the risk of damage to the sensor. Due to the $1/r^2$ falloff from the central region of the PSF, vortex-encoded images experience a larger saturation "ring" where the signal is unrecoverable. Areas of saturation cause ringing and image reconstruction errors after image processing. By using higher-order phase elements, the maximum irradiance can be sufficiently decreased such that saturation can be minimized or avoided completely. We found that for the highest-order phase masks used in this work, the Wiener deconvolution was able to recover higher spatial frequencies with the axicon pupil phase function than the vortex pupil phase function. Due to less saturation for low-order phase masks and better spatial frequency recovery for high-order phase masks, the axicon-encoded phase masks performed better than the vortex phase mask. Despite the performance gains, the reader should be reminded that the axicon encoding requires a larger format/area sensor to avoid clipping/losing light from the out-of-focus irradiance in the detector plane when the phase mask is present. In an operational environment, the trade-off space between image resolution, area of image saturation and/or sensor damage, laser suppression ratio, and sensor size are all factors that need to be considered when choosing an appropriate phase mask. With the presence of zeros in both resulting MTF functions, additional work needs to be performed to look at other families and classes of phase masks that jointly optimize the criteria of coherent PSF suppression and incoherent image reconstruction for the application of minimizing the risk of laser damage to image sensors.

9 Future Work

The paper compares vortex and axicon pupil phase mask encoding for a recorded image having both coherent and incoherent contributions. We will continue to explore

alternative phase masks that maximize the goals described in Sec. 2. Alternative designs may include superposition of vortex and/or axicon phase masks. Initial computational studies suggest that vortex and axicon phases perform well compared to other options, including random masks and Zernike polynomials. Additionally, we are working toward a system prototype using these higher-order masks. Several groups have developed techniques to fabricate high-order phase masks. Higher-order masks can be produced with a binary holographic pattern fabricated through nanolithography (see, e.g., Ref. 18). Commercial broadband q-plates can be manufactured with vortex charges up to $m = 128$.[19] Shen et al.[20] have fabricated spiral phase mirrors from direct machining with an ultraprecision single point diamond turning lathe with vortex charges up to $m = 5050$. These various techniques provide a basis for fabricating phase masks for a future system prototype.

Acknowledgments

Sources of funding include Naval Research Laboratory, National Science Foundation Grant No. ECCS-1309517 and Office of Naval Research Grant No. N00014-16-1-2114, N0001416-WX-0-0165, and N00014160-WX-0-0022.

References

1. E. R. Dowski and W. T. Cathey, "Extended depth of field through wavefront coding," *Appl. Opt.* **34**(11), 1859–1866 (1995).
2. W. T. Cathey and E. R. Dowski, "New paradigm for imaging systems," *Appl. Opt.* **41**(29), 6080–6092 (2002).
3. N. Cohen et al., "Enhancing the performance of the light field microscope using wavefront coding," *Opt. Express* **22**(20), 24817–24839 (2014).
4. R. M. A. Schleijpen et al., "Laser dazzling of focal plane array cameras," *Proc. SPIE* **6738**, 67380O (2007).
5. M. F. Becker et al., "Laser-induced functional damage to silicon CCD sensor arrays," *Proc. SPIE* **1624**, 67–79 (1992).
6. Y. P. Sun and J. E. Riggs, "Organic and inorganic optical limiting materials. From fullerenes to nanoparticles," *Int. Rev. Phys. Chem.* **18**(1), 43–90 (1999).
7. L. W. Tutt and T. F. Boggess, "A review of optical limiting mechanisms and devices using organics, fullerenes, semiconductors and other materials," *Prog. Quantum Electron.* **17**(4), 299–338 (1993).
8. E. W. Van Stryland et al., "Optical limiting with semiconductors," *J. Opt. Soc. Am. B* **5**(9), 1980–1989 (1988).
9. K. Mansour, M. J. Soileau, and E. W. Vanstryland, "Nonlinear optical-properties of carbon-black suspensions (ink)," *J. Opt. Soc. Am. B* **9**(7), 1100–1109 (1992).
10. G. J. Ruane, A. T. Watnik, and G. A. Swartzlander, "Reducing the risk of laser damage in a focal plane array using linear pupil-plane phase elements," *Appl. Opt.* **54**(2), 210–218 (2015).
11. V. V. Kotlyar et al., "Diffraction of a plane, finite-radius wave by a spiral phase plate," *Opt. Lett.* **31**(11), 1597–1599 (2006).
12. V. V. Kotlyar et al., "Diffraction of a finite-radius plane wave and a Gaussian beam by a helical axicon and a spiral phase plate," *J. Opt. Soc. Am. A* **24**(7), 1955–1964 (2007).
13. Z. S. Sacks, D. Rozas, and G. A. Swartzlander, "Holographic formation of optical-vortex filaments," *J. Opt. Soc. Am. B* **15**(8), 2226–2234 (1998).
14. J. A. Nelder and R. Mead, "A simplex method for function minimization," *Comput. J.* **7**(4), 308–313 (1965).
15. J. C. Lagarias et al., "Convergence properties of the Nelder–Mead simplex method in low dimensions," *SIAM J. Optim.* **9**(1), 112–147 (1998).
16. G. A. Swartzlander, "The optical vortex coronagraph," *J. Opt. A: Pure Appl. Opt.* **11**(9), 094022 (2009).
17. D. J. Brady, *Optical Imaging and Spectroscopy*, Wiley, Optical Society of America, Hoboken, New Jersey (2009).
18. G. J. Ruane et al., "Vortex-phase filtering technique for extracting spatial information from unresolved sources," *Appl. Opt.* **53**(20), 4503–4508 (2014).
19. Beam Co., http://www.beamco.com/Vector-Vortex-Waveplates-VVW-.
20. Y. Shen et al., "Generation and interferometric analysis of high charge optical vortices," *J. Opt.* **15**(4), 044005 (2013).

Abbie T. Watnik is a research physicist at the U.S. Naval Research Laboratory in the Optical Sciences Division. She received her BS degree in electrical engineering from Colorado State University in 2006 and her MS and PhD degrees in optics from the University of Rochester in 2010 and 2012, respectively. Her current research interests include digital holography, wavefront coding and image reconstruction techniques. She is a member of SPIE.

Garreth J. Ruane is currently a postdoctoral researcher in the Astronomy Department, California Institute of Technology, and a member of SPIE. He received his PhD from Chester F. Carlson Center for Imaging Science at Rochester Institute of Technology (RIT) in May 2016. His research interests include high-contrast imaging techniques and instrumentation for the detection and characterization of exoplanets.

Grover A. Swartzlander is an associate professor at Chester F. Carlson Center for Imaging Science, RIT. He received his PhD in 1990 from Johns Hopkins University and has taught physics and optics at the Worcester Polytechnic Institute and the University of Arizona before coming to RIT in 2008. His research interests include high-contrast imaging for exoplanet detection, computational imaging, and radiation pressure techniques for future solar sailing missions. He is a member of SPIE and a fellow of the OSA.